



AFRL-RX-WP-JA-2014-0214

STRUCTURE AND OPTICAL PROPERTIES OF NANOCRYSTALLINE HAFNIUM OXIDE THIN FILMS (POSTPRINT)

**Neil R. Murphy
AFRL/RXAP**

**SEPTEMBER 2014
Interim Report**

Distribution A. Approved for public release; distribution unlimited.

See additional restrictions described on inside pages

STINFO COPY

© 2014 Elsevier B.V.

**AIR FORCE RESEARCH LABORATORY
MATERIALS AND MANUFACTURING DIRECTORATE
WRIGHT-PATTERSON AIR FORCE BASE, OH 45433-7750
AIR FORCE MATERIEL COMMAND
UNITED STATES AIR FORCE**

NOTICE AND SIGNATURE PAGE

Using Government drawings, specifications, or other data included in this document for any purpose other than Government procurement does not in any way obligate the U.S. Government. The fact that the Government formulated or supplied the drawings, specifications, or other data does not license the holder or any other person or corporation; or convey any rights or permission to manufacture, use, or sell any patented invention that may relate to them.

This report was cleared for public release by the USAF 88th Air Base Wing (88 ABW) Public Affairs Office (PAO) and is available to the general public, including foreign nationals.

Copies may be obtained from the Defense Technical Information Center (DTIC)
(<http://www.dtic.mil>).

AFRL-RX-WP-JA-2014-0214 HAS BEEN REVIEWED AND IS APPROVED FOR PUBLICATION IN ACCORDANCE WITH ASSIGNED DISTRIBUTION STATEMENT.

//Signature//

NEIL R. MURPHY
Photonic Materials Branch
Functional Materials Division

//Signature//

CHRISTOPHER D. BREWER, Chief
Photonic Materials Branch
Functional Materials Division

//Signature//

TIMOTHY J. BUNNING, Chief
Functional Materials Division
Materials and Manufacturing Directorate

This report is published in the interest of scientific and technical information exchange, and its publication does not constitute the Government's approval or disapproval of its ideas or findings.

REPORT DOCUMENTATION PAGE

*Form Approved
OMB No. 074-0188*

Public reporting burden for this collection of information is estimated to average 1 hour per response, including the time for reviewing instructions, searching existing data sources, gathering and maintaining the data needed, and completing and reviewing this collection of information. Send comments regarding this burden estimate or any other aspect of this collection of information, including suggestions for reducing this burden to Defense, Washington Headquarters Services, Directorate for Information Operations and Reports, 1215 Jefferson Davis Highway, Suite 1204, Arlington, VA 22202-4302. Respondents should be aware that notwithstanding any other provision of law, no person shall be subject to any penalty for failing to comply with a collection of information if it does not display a currently valid OMB control number. PLEASE DO NOT RETURN YOUR FORM TO THE ABOVE ADDRESS.

| | | | | | | |
|--|--|--|--|--|---|--|
| 1. REPORT DATE (DD-MM-YYYY) September 2014 | | | 2. REPORT TYPE Interim | | 3. DATES COVERED (From – To) 06 May 2010 – 14 August 2014 | |
| 4. TITLE AND SUBTITLE STRUCTURE AND OPTICAL PROPERTIES OF NANOCRYSTALLINE HAFNIUM OXIDE THIN FILMS (POSTPRINT) | | | 5a. CONTRACT NUMBER In-House | | | |
| | | | 5b. GRANT NUMBER | | | |
| | | | 5c. PROGRAM ELEMENT NUMBER 62102F | | | |
| 6. AUTHOR(S) (see back) | | | 5d. PROJECT NUMBER 4348 | | | |
| | | | 5e. TASK NUMBER | | | |
| | | | 5f. WORK UNIT NUMBER X09X | | | |
| 7. PERFORMING ORGANIZATION NAME(S) AND ADDRESS(ES) (see back) | | | 8. PERFORMING ORGANIZATION REPORT NUMBER | | | |
| | | | 10. SPONSOR/MONITOR'S ACRONYM(S) AFRL/RXAP | | | |
| 9. SPONSORING / MONITORING AGENCY NAME(S) AND ADDRESS(ES) Air Force Research Laboratory Materials and Manufacturing Directorate Wright Patterson Air Force Base, OH 45433-7750 Air Force Materiel Command United States Air Force | | | 11. SPONSOR/MONITOR'S REPORT NUMBER(S) AFRL-RX-WP-JA-2014-0214 | | | |
| | | | 12. DISTRIBUTION / AVAILABILITY STATEMENT Distribution A. Approved for public release; distribution unlimited. This report contains color. | | | |
| 13. SUPPLEMENTARY NOTES PA Case Number: 88ABW-2014-2201; Clearance Date: 09 May 2014. Journal article published in Optical Materials 37 (2014) 621-628. © 2014 Elsevier B.V.. The U.S. Government is joint author of the work and has the right to use, modify, reproduce, release, perform, display or disclose the work. The final publication is available at http://dx.doi.org/10.1016/j.optmat.2014.08.005 | | | | | | |
| 14. ABSTRACT Hafnium oxide (HfO ₂) films were grown by sputter-deposition by varying deposition temperature (T _s) in a wide range of 25–700°C. The deposited HfO ₂ films were characterized by studying their growth behavior, microstructure, and optical properties. Characterization of the films employing a wide range of analytical techniques indicate a clear functional relationship between processing conditions, structure, morphology, and optical properties. HfO ₂ films were amorphous at T _s < 200°C, at which point a structural transformation occurs. HfO ₂ films grown at T _s < 200°C were nanocrystalline, stabilized in a monoclinic structure. The nanocrystalline HfO ₂ films exhibit a strong (111) texturing. The average crystallite size of HfO ₂ films increased from ~10 nm to ~20 nm with increasing T _s . Electron and atomic force microscopy measurements also correlated with the crystalline behavior, as well as an evenly distributed network of spherical shaped crystallites for the nanocrystalline HfO ₂ films. Density (ρ) of HfO ₂ films probed using X-ray reflectivity and ellipsometry data analysis indicate that the ρ values are strongly dependent on T _s ; ρ varied in the range of 7.36–9.14 g/cm ³ . The higher end of ρ values were noted only for HfO ₂ films grown at relatively higher T _s indicating the crystalline nature accounts for the ρ improvement. The band gap values of the films varied in the range of 5.78–6.17 (±0.03) eV for T _s = 25–700°C. Index of refraction at 550 nm increased from 1.80 to 2.09, which also correlates with the characteristic feature of improved structural order, packing density of HfO ₂ films with increasing T _s . Based on the observed results, a correlation between growth conditions, microstructure and optical constants is established. | | | | | | |
| 15. SUBJECT TERMS hafnium oxide, sputter-deposition, structure, XRR, optical properties, ellipsometry | | | | | | |
| 16. SECURITY CLASSIFICATION OF: a. REPORT Unclassified | | 17. LIMITATION OF ABSTRACT SAR | 18. NUMBER OF PAGES 12 | 19a. NAME OF RESPONSIBLE PERSON (Monitor) Neil R. Murphy | | |
| | | | | 19b. TELEPHONE NUMBER (include area code) (937) 255-1829 | | |

REPORT DOCUMENTATION PAGE Cont'd

6. AUTHOR(S)

Neil R. Murphy - Materials and Manufacturing Directorate, Air Force Research Laboratory, Functional Materials Division

M. Vargas - Department of Metallurgical and Materials Engineering, University of Texas at El Paso

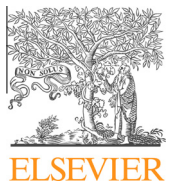
C.V. Ramana - Department of Mechanical Engineering, University of Texas at El Paso

7. PERFORMING ORGANIZATION NAME(S) AND ADDRESS(ES)

AFRL/RXAP
Air Force Research Laboratory
Materials and Manufacturing Directorate
Wright-Patterson Air Force Base, OH 45433-7750

Department of Metallurgical and Materials Engineering
University of Texas at El Paso
El Paso, TX 79968

Department of Mechanical Engineering
University of Texas at El Paso
El Paso, TX 79968



Structure and optical properties of nanocrystalline hafnium oxide thin films

M. Vargas ^a, N.R. Murphy ^b, C.V. Ramana ^{c,*}

^a Department of Metallurgical and Materials Engineering, University of Texas at El Paso, El Paso, TX 79968, USA

^b Materials and Manufacturing Directorate (RX), 3005 Hobson Way, Wright-Patterson Air Force Base (WPAFB), Dayton, OH 45433, USA

^c Department of Mechanical Engineering, University of Texas at El Paso, El Paso, TX 79968, USA

ARTICLE INFO

Article history:

Received 26 May 2014

Received in revised form 30 July 2014

Accepted 14 August 2014

Available online 17 September 2014

Keywords:

Hafnium oxide

Sputter-deposition

Structure

XRR

Optical properties

Ellipsometry

ABSTRACT

Hafnium oxide (HfO_2) films were grown by sputter-deposition by varying deposition temperature (T_s) in a wide range of 25–700 °C. The deposited HfO_2 films were characterized by studying their growth behavior, microstructure, and optical properties. Characterization of the films employing a wide range of analytical techniques indicate a clear functional relationship between processing conditions, structure, morphology, and optical properties. HfO_2 films were amorphous at $T_s \leq 200$ °C, at which point a structural transformation occurs. HfO_2 films grown at $T_s \geq 200$ °C were nanocrystalline, stabilized in a monoclinic structure. The nanocrystalline HfO_2 films exhibit a strong (111) texturing. The average crystallite size of HfO_2 films increased from ~10 nm to ~20 nm with increasing T_s . Electron and atomic force microscopy measurements also correlated with the crystalline behavior, as well as an evenly distributed network of spherical shaped crystallites for the nanocrystalline HfO_2 films. Density (ρ) of HfO_2 films probed using X-ray reflectivity and ellipsometry data analysis indicate that the ρ values are strongly dependent on T_s ; ρ varied in the range of 7.36–9.14 g/cm³. The higher end of ρ values were noted only for HfO_2 films grown at relatively higher T_s indicating the crystalline nature accounts for the ρ improvement. The band gap values of the films varied in the range of 5.78–6.17(±0.03) eV for $T_s = 25$ –700 °C. Index of refraction at 550 nm increased from 1.80 to 2.09, which also correlates with the characteristic feature of improved structural order, packing density of HfO_2 films with increasing T_s . Based on the observed results, a correlation between growth conditions, microstructure and optical constants is established.

© 2014 Elsevier B.V. All rights reserved.

1. Introduction

Hafnium oxide (HfO_2) is a technologically important metal oxide, which is characterized by a unique combination of mechanical, chemical, electronic and optical properties [1–15]. HfO_2 films exhibit high dielectric constant ($k \sim 25$) and wide band gap ($E_g \sim 5.7$ eV), which makes the material attractive for applications in the fields of electronics and opto-electronics [1–4]. HfO_2 remains the leading candidate to replace SiO_2 dielectrics in gate oxides due to a higher permittivity and reportedly lower electron tunneling effects [5,6].

Hafnium oxide exhibits various polymorphs on the basis of temperature and pressure. Monoclinic HfO_2 ($P2_1/C$) is the most thermodynamically stable phase at ambient conditions of temperature and pressure [7,8]. At temperatures higher than 1700 °C,

HfO_2 transforms into the tetragonal ($P4_2/nmc$) phase [7]. A further increase to 2200 °C results in the cubic ($Fm\bar{3}m$) phase formation [7]. In addition, monoclinic HfO_2 may undergo a phase transition under pressures of the order of 12 GPa to a denser structure, orthorhombic I ($Pbca$), and a further increase in pressure to 28 GPa results in the orthorhombic II ($Pnma$) phase formation [7,8]. In view of the set of thermodynamic conditions resulting in specific phase formation and properties, the controlled growth and manipulation of specific crystal structures at the nanoscale dimensions have important implications for the design and applications of HfO_2 . The present work is focused towards the fabrication, structural analysis and optical property evaluation of nanocrystalline HfO_2 films by sputter-deposition.

A large band gap coupled with low absorption provide optical transparency over a broad range in the electromagnetic spectrum; HfO_2 optical films and coatings can operate efficiently down to 220 nm in the ultraviolet (UV) region and 10 μm in the infrared (IR) region [9,10]. There are not many contenders that are stable

* Corresponding author.

E-mail address: rvcintalapalle@utep.edu (C.V. Ramana).

under UV considerations, therefore HfO₂ is also a preferred high index material when high laser damage threshold is a requirement. As a result, HfO₂ has been used in optical coating applications, including optical filters, ultraviolet heat mirrors, antireflection coatings and novel scintillation materials [1–12].

The objective of the present work is to derive a comprehensive understanding of the structure and optical properties of HfO₂ thin films grown as a function of variable deposition temperature. Often, very specific film properties are required for optimal performance. It is evident, and well known, that the thermodynamically stability and phase existence depends on growth temperature and pressure conditions. In addition, the controlled growth and manipulation of specific HfO₂ crystal structures at the nanoscale dimensions is the driving force for technological implications. Therefore, it is important to characterize and obtain a correlation between physico-chemical and optical properties in nanocrystalline HfO₂ films as a function of growth conditions. Most importantly, determining the optical properties such as band gap (E_g), index of refraction (n) is important for transparent oxides, such as HfO₂ in this case. Furthermore, for thin films and nanomaterials, ' E_g ' and ' n ' values are sensitive to the microstructure; *optical parameters* are influenced by various factors such as surface/interface structure, crystal quality, packing density, lattice parameters, and defect structure. On the other hand, tailoring E_g and spectral behavior of ' n ' and the dispersion profiles allows for engineering modern electronic and optical devices. In this work, HfO₂ films were produced by sputter-deposition in a wide range of growth temperature, which results in HfO₂ films with a variable microstructure. The preliminary results of spectroscopic ellipsometry characterization of the index of refraction for HfO₂ films has been reported elsewhere [13]. The effect of growth temperature on the optical properties is reported and a structure–property relationship is established in this paper for HfO₂ sputter-deposited films.

2. Experimental

2.1. Film growth

Hafnium oxide films were deposited onto silicon (100) wafers and quartz substrates by radio frequency magnetron sputtering. All the substrates were thoroughly cleaned and dried with nitrogen before introducing them into the vacuum chamber, which was initially evacuated to a base pressure of $\sim 10^{-6}$ Torr. A hafnium (Hf) target (Plasmatec, Inc.) of 2 in. diameter and 99.95% purity was employed for sputtering. The Hf target was placed on a 2 in. sputter gun, which is placed at a distance of 8 cm from the substrate. The sputtering gas was high-purity (99.999%) argon (Ar), while oxygen (O₂) was introduced during deposition for reactive growth to form Hf-oxide. A power of 100 W was employed for reactive deposition. The ratio of Ar to O₂ was kept at 70:30 (28 sccm Ar mixed with 12 sccm of O₂), and the respective flow of each gas was monitored using an MKS mass flow meter. Before each deposition, the Hf target was pre-sputtered for 10 min with a shutter above the gun closed. The deposition time was carried out for 45 min. The thicknesses of the films were in the range ~ 33 –60 nm. Film thickness measurements were made by three different methods as discussed under Section 3. Growth temperature (T_s) was varied in the range of room temperature (RT = 25 °C)–700 °C, the other variables such as sputtering power, pressure, and flow of Ar and O₂ and their ratio were kept constant.

2.2. Characterization

The grown HfO₂ films were characterized by performing crystal structure, surface morphology, and optical measurements.

2.2.1. X-ray diffraction (XRD)

X-ray diffraction (XRD) measurements on HfO₂ films grown on Si were performed using a Bruker D8 Advance X-ray diffractometer. All the measurements were made ex situ as a function of growth temperature. In order to avoid interference by the substrate and obtain diffraction pattern of the coatings, grazing incidence X-ray diffraction (GIXRD) were performed on the films. XRD patterns were recorded using Cu K α radiation ($\lambda = 1.54056$ Å) at room temperature. High resolution scans were also performed on evident crystallization peaks with parameter of a step size of 0.01° per 1 s. The crystalline domain size was calculated through the use of the Scherrer relationship, after removal of background artifacts. The Scherrer equation is defined by,

$$D_{hkl} = 0.9\lambda/\beta \cos \theta \quad (1)$$

where D_{hkl} is the crystallite size, λ is the wavelength of the filament used in the XRD machine, β is the full width half maximum of the peak corrected for instrumental broadening, and θ is the angle of the peak [16,17].

2.2.2. Scanning electron microscopy (SEM)

Surface imaging analysis was performed using a high-performance and ultra-high resolution scanning electron microscope (Hitachi S-4800). Secondary electron imaging was performed on HfO₂ films grown on Si wafers using carbon paste at the ends to avoid charging problems.

2.2.3. Atomic force microscopy (AFM)

Surface morphology of the HfO₂ films was also studied employing atomic force microscopy (AFM) using a Veeco Multimode scanning probe microscope with a Nanoscope V controller. AFM images were acquired using the ScanAsyst mode which utilizes a Bruker proprietary method for curve collection and sophisticated algorithms to continuously monitor image quality, and automatically make appropriate parameter adjustments [18]. Aluminum coated silicon cantilevers (Bruker, USA) were used to acquire ScanAsyst mode images. The cantilevers measure 115 μm long, 25 μm wide and 0.65 μm thick with a spring constant of 0.4 N/m a resonance frequency of 70 kHz. Tip quality was qualitatively assessed by the clarity and presence of artifacts in the acquired images. The calibration standard used to calibrate the scanner consisted of platinum-coated, 200 nm-tall silicon columns spaced at 10 μm intervals on centers. The columns have a length of 5 nm on a side.

AFM images (512 scan lines & 512 pixels per scan line) were acquired with an integral gain of approximately 2, a proportional gain of approximately 50, and an amplitude setpoint of 200 mV. The drive amplitude varied between 30 and 180 mV. The images were then subjected to a 3rd order flattening procedure using the Veeco Nanoscope software to remove the non-linear background artifact introduced by the piezo scanner. Following the flattening procedure, the surface roughness was quantified over five areas of 1 μm × 1 μm on the 5 μm × 5 μm scan size images.

2.2.4. X-ray reflectivity (XRR)

X-ray reflectometry (XRR) measurements were performed on a Rigaku Smartlab X-ray diffractometer. A Cu K α X-ray source is used by the Smartlab diffractometer. Scans were taken at a speed of 0.2° per minute and a step size of 0.005°. The total length of scans were taken at low angles from 0° to 6°. Experimental data was then fit with the software package GlobalFit associated with Rigaku Smartlab diffractometer.

2.2.5. Spectrophotometry measurements

Optical properties were evaluated using both spectrophotometric and ellipsometry measurements. Spectrophotometry measurements were attained by using a Cary 5000 UV-vis-NR

double-beam spectrophotometer. Films grown on optical grade quartz were employed for optical property measurements to probe the transparent nature and band gap analysis of the HfO_2 films.

2.2.6. Spectroscopic ellipsometry (SE)

Spectroscopic ellipsometry (SE) was performed ex-situ on the films grown on silicon wafers by utilizing a J.A. Woollam V-VASE instrument. Measurements were done in the range of 300–1350 nm with a step size of 2 nm and at angles of incidence of 65°, 70°, and 75°, near the Brewster's angle of silicon. The ellipsometry data analysis was performed using commercially available WVASE32 software.

3. Results and discussion

3.1. Crystal structure

X-ray diffraction patterns of HfO_2 films are shown in Fig. 1a as a function of T_s . The patterns at $T_s \geq 200^\circ\text{C}$ exhibit crystalline nature oriented along the $(\bar{1}11)$, designating a crystallization temperature of 200°C for monoclinic HfO_2 . The film remains amorphous for $T_s = \text{RT}$. However, the peak corresponding to $T_s = 200^\circ\text{C}$ is minor and broad. Perhaps, small crystallites being present in an amorphous matrix might be the reason for appearance of the broad peak. The intensity of the $(\bar{1}11)$ peak increases with increasing growth temperature which indicates an increase in crystallite size with T_s . The films exhibit a strong $(\bar{1}11)$ texturing which is expected based on phase-stability considerations [19–24]. It is well-known that $(\bar{1}11)$ planes will primarily populate as they exhibit the lowest surface free energy, although minor peaks due to other orientations of monoclinic crystallites are also present at

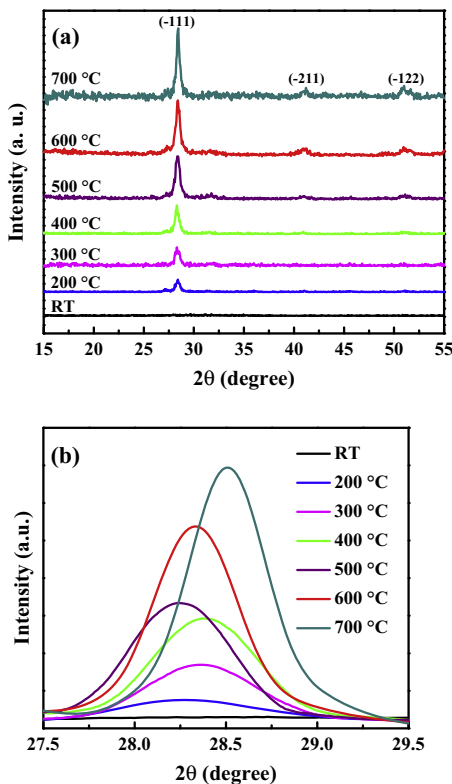


Fig. 1. (a) GIXRD patterns of the HfO_2 films grown as a function of temperature. The films crystallize preferentially in $(\bar{1}11)$ monoclinic orientation. (b) High-resolution scans of the $(\bar{1}11)$ peaks.

higher temperatures. High resolution scans of $(\bar{1}11)$ texturing are shown in Fig. 1b. The high resolution scans were performed on $(\bar{1}11)$ peaks for all the HfO_2 films in order to obtain further information on the growth process, phase, and crystallite size at the nanoscale dimensions. It can be noted that the peak shifts to the higher diffracting angle for films grown from 200°C to 400°C . This trend continues for films grown at higher temperatures, however, at 500°C the peak position retrogrades before continuing to increase. The shift in peak position is attributed to the lattice expansion and lattice mismatch between film and substrate. It is important to recognize the variation of d spacing for $(\bar{1}11)$ planes with T_s which aids in obtaining quantitative information on the lattice expansion. The d spacing versus T_s for HfO_2 films is shown in Fig. 2. The trend in $d(\bar{1}11)$ is increasing for $T_s \leq 400^\circ\text{C}$, after which the trend begins to slightly decline for $T_s \geq 500^\circ\text{C}$. This leads to conclude that in this regime of T_s the lattice mismatch is at a maximum [20]. It is evident that at $T_s \geq 500^\circ\text{C}$, the increase in grain size is affected more by the microstrain in the thin films, and slightly less by the effect of temperature. The average crystallite size increased from $\sim 10\text{ nm}$ to $\sim 20\text{ nm}$ ($\pm 2\text{ nm}$) with increasing T_s from 200 to 700°C . Furthermore, FWHM values decrease with T_s attributing to the increase in crystallite size (Fig. 2).

3.2. Film thickness and density

The XRR data of HfO_2 films are shown in Fig. 3. Simulation of the XRR experimental data using appropriate models can provide physio-chemical information of HfO_2 films. Specifically, the surface roughness, thickness and density of the HfO_2 films can be obtained from XRR spectra [22]. The density can be calculated from the total reflection or critical edge, while film thickness can be derived from the period of the oscillations in the XRR spectra. In the present case, it is evident that the experimental and simulation curves are in excellent agreement for HfO_2 films (Fig. 3). The stack model employed to simulate the XRR spectra contains, from top, HfO_2 film, SiO_2 interface and Si substrate. The surface and interface roughness were also considered in order to accurately fit the experimental XRR spectra of HfO_2 films. A positive shift of the critical edge noted from XRR spectra indicates that the film density increases with T_s ; further analysis was made with SE measurements as explained in the later portion of the discussion. The period of the oscillations present for the crystalline samples of the HfO_2 films does not significantly change with T_s , which is in agreement with the deposition rate to obtain $\sim 40\text{ nm}$ thicknesses;

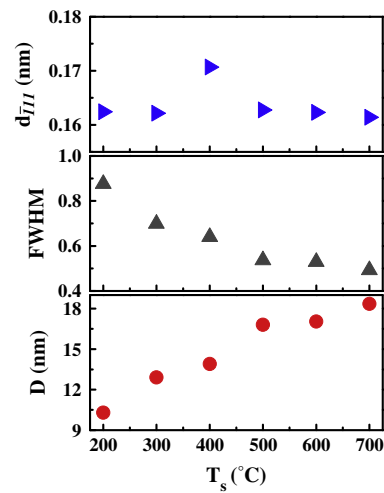


Fig. 2. Variation of $d(\bar{1}11)$ spacing, FWHM, and D (crystallite size) with T_s .

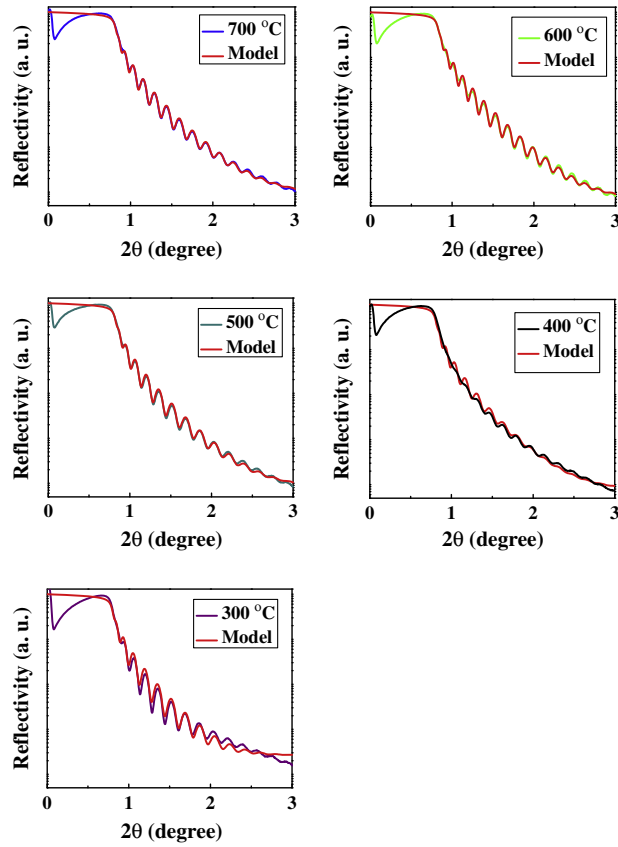


Fig. 3. Measured reflectivity curves for HfO_2 films grown at various temperatures. The experimental data and model curves are shown for samples grown at $T_s = 300$, 400, 500, 600, and 700 °C.

thickness measurements will also be validated with SEM and SE measurements discussed below. Thickness measurements observed were for the fully crystallized films ($T_s = 300$ –700 °C). Structural information obtained for the HfO_2 films is demonstrated in Fig. 4.

3.3. Surface morphology

The scanning electron microscopy (SEM) images of the HfO_2 films are shown in Fig. 5. The amorphous nature of the film is evident in the sample grown at RT. The crystalline samples ($T_s = 200$ –700 °C) possess a uniform distribution of dense particles spherical in shape. Topographical features of the HfO_2 films are also correlated through AFM and shown in Fig. 6. Most importantly an evident decrease in peak to valley or surface height with increase in growth temperature yields a roughness profile. The root-mean-square (rms) roughness of HfO_2 films decreases as T_s increases as seen in Fig. 7. Roughness measurements are evidently related to the quality of the films. A smoother film will occupy fewer reaction sites and promote minimal interfacial reactions between the HfO_2 film and Si substrate. Fig. 7 demonstrates a correlation between XRR roughness measurements and AFM roughness profiling which are well in agreement with one another.

3.4. Spectral transmission characteristics and band gap

Having established the microstructural and physical qualities of the HfO_2 films, the attention is now directed to the optical nature of the films. The HfO_2 films were transparent and colorless under transmitted light down to the 200 nm wavelength range as seen

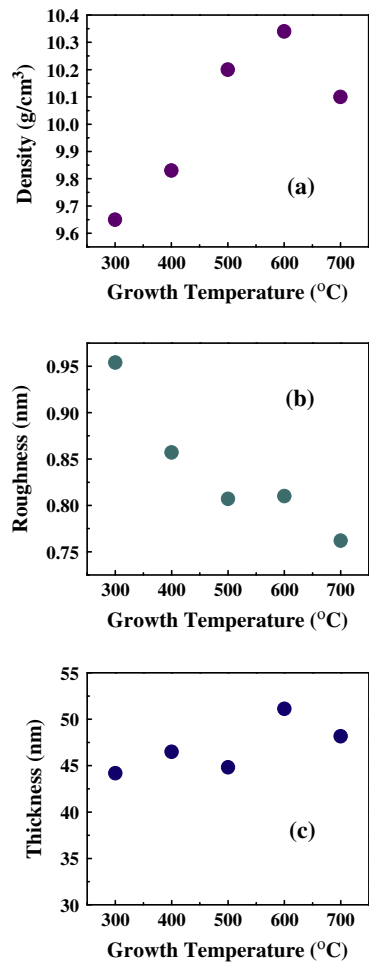


Fig. 4. (a) Density of the HfO_2 films grown at various temperatures. (b) Surface roughness of the films at various temperatures. (c) Thickness of the films.

in Fig. 8a. The highest transparency is observed by the amorphous film over a wide wavelength range (200–800 nm) ranging from 85% to 95% at lower wavelengths. The monoclinic polycrystalline films still employ transparencies of near 70% at lower wavelengths but significantly less than the amorphous film. A further analysis of the optical spectra is performed to better understand the effect of microstructure on the optical properties and to derive a quantitative structure–property relationship. The optical absorption coefficient, α , of the films is evaluated using the relation:

$$\alpha = [-1/t] \ln[T/(1-R)^2] \quad (2)$$

where T is the transmittance, R is the reflectance, and t is the film thickness [10,25–29]. Absorption data for the films grown at $T_s = \text{RT}$ –700 °C can be seen in Fig. 8b. An interesting observation to be made from the absorption data is the shoulder-like feature provided by the crystalline films. This feature is strongly correlated with the crystallization of amorphous HfO_2 [28].

Further absorption data analysis was made to understand the broad energy feature and determine band gap measurements. Band gap values for the HfO_2 films were measured by employing the power law of the form:

$$\alpha h\nu = B(h\nu - E_g)^n \quad (3)$$

where $h\nu$ is the incident photon, α is the absorption coefficient, B is the absorption edge width parameter, E_g is the band gap, and n is the exponent dependent on direct or indirect intrinsic band gap behavior [10,25–29]. The indirect band gap value for HfO_2 is related

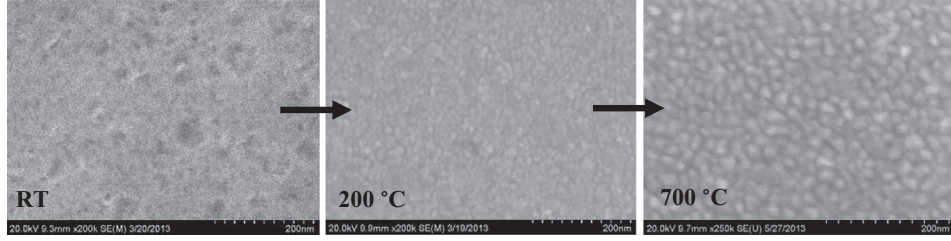


Fig. 5. SEM images of the HfO₂ films demonstrating structural change in film morphology as the films go from amorphous to monoclinic, emphasizing the effect of T_s .

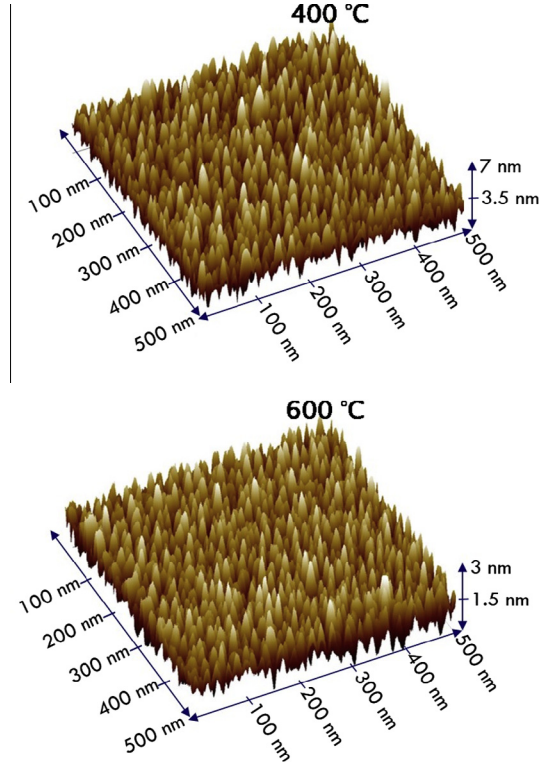


Fig. 6. AFM images for representative nanocrystalline HfO₂ films demonstrating topographical film features as well as a decrease in surface height with T_s .

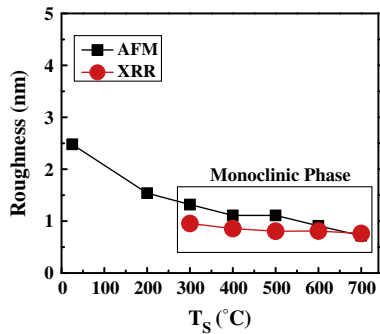


Fig. 7. Film roughness measurements obtained through AFM measurements and XRR data fitting analysis. The trend for roughness measurements is decreasing for both methods of characterization, which attribute to the overall quality in the films.

to the electronic transition from the O 2p valence band to the Hf 5d conduction band between Γ and B points on the reciprocal lattice of monoclinic HfO₂ [27,28]. Indirect band gap measurements were made following the power law with $n = 1/2$ on the band that initiates at 5.6 eV for the crystalline films as seen in Fig. 9. The existence

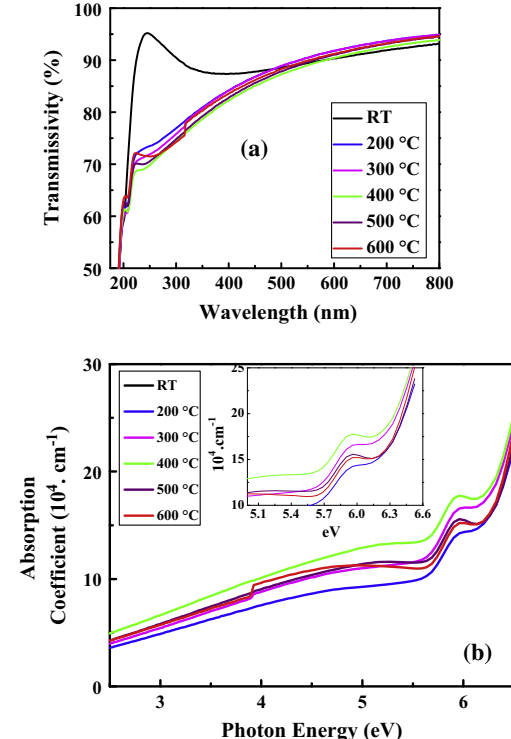


Fig. 8. Transmittance spectra for the HfO₂ films. The amorphous films is highly transparent, and even more so at lower wavelengths. The absorption spectra for the films demonstrate a low energy shoulder as a consequence of HfO₂ crystallization.

of the additional absorption band will initiate and saturate below E_g of the films [27]. Extrapolating the linear region of the $(\chi h\nu)^{1/2}$ plot to zero and regression analysis for R^2 values greater than 0.9 provide accurate indirect- E_g values which ultimately reveal a decreasing trend with T_s . Looking at the absorption coefficient for the films exhibiting monoclinic orientations ($T_s = 200$ –600 °C) at values higher than 6.00 eV (inset of Fig. 8b) the steepest increase in absorption is observed. The high energies coupled with high absorption behavior tailor to band-band transitions, and therefore E_g has been measured by following the direct band gap power law with $n = 2$ [26,29–32]. Extrapolating the linear region of the plot to zero and regression analysis for R^2 values greater than 0.9 provide accurate E_g values as seen in Fig. 10. The band gap values are increasing with increasing T_s as observed in Fig. 10 in the range of 5.75–6.13 eV. The more notable factor is the impact of the amorphous to monoclinic transition which causes a significant change in band gap measurements.

3.5. Optical constants

Ultimately, the optical constants of the nanocrystalline, monoclinic HfO₂ films are considered and discussed. Optical constants

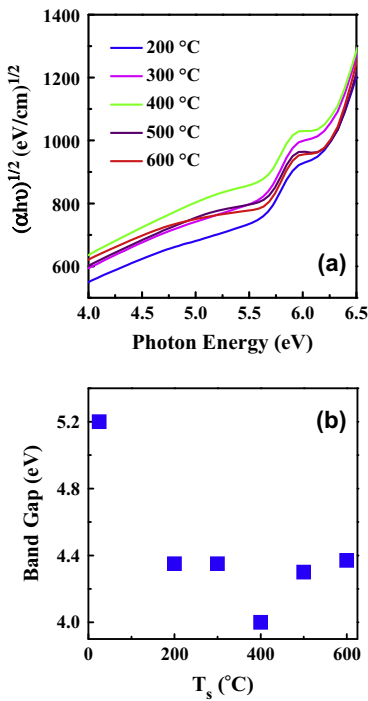


Fig. 9. (a) $(\alpha h\nu)^{1/2}$ vs photon energy for individual HfO_2 films grown at different temperatures. (b) The indirect E_g values were obtained by extrapolating the linear region of the band that initiates at ~ 5.6 eV.

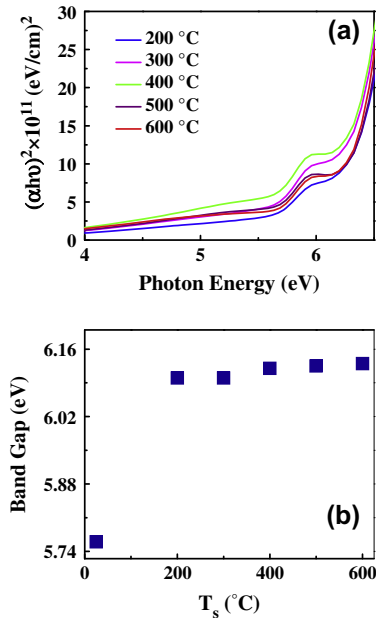


Fig. 10. (a) $(\alpha h\nu)^2$ vs photon energy for individual HfO_2 films grown at different temperatures. The effect of amorphous to monoclinic transition is well defined in the values. (b) E_g variation with T_s . It can be noted that E_g values are increasing with T_s .

of the HfO_2 films were primarily probed by SE, which measures the relative changes in the amplitude and phase of the linearly polarized monochromatic incident light upon oblique reflection from the sample surface. The experimental parameters obtained by SE are the angles Ψ (azimuth) and Δ (phase change), which are related to the microstructure and optical properties, defined by:

$$\rho = R_p/R_s = \tan \Psi \exp(i\Delta) \quad (4)$$

where R_p and R_s are the complex reflection coefficients of the light polarized parallel and perpendicular to the plane of incidence, respectively [33–36]. In general, the fundamental equation of ellipsometry that relates the measurable with the accessible optical information is:

$$\rho = \tan \Psi \exp(i\Delta) = \rho(N_0, N_1, N_2, L_1, \Phi_0, \lambda) \quad (5)$$

where the middle term contains the measurable and the last term on the right contains all the accessible parameters of the measurement, namely, film thicknesses, optical properties, the wavelength of light, and the angle of incidence [35]. The spectral dependencies of ellipsometric parameters Ψ (azimuth) and Δ (phase change) can be fitted with appropriate models to extract film thickness and the optical constants i.e., the refractive index (n) and extinction coefficient (k), based on the best fit between experimental and simulated spectra [25,33–36]. In the present case, the Levenberg–Marquardt regression algorithm was used for minimizing the mean-squared error (MSE):

$$\text{MSE} = \frac{1}{2N - M} \sum_{i=1}^n \left[\left\{ \frac{(\Psi_{\text{exp}} - \Psi_{\text{calc}})}{\sigma_{\Psi_i}^{\text{exp}}} \right\}^2 + \left\{ \frac{(\Delta_{\text{exp}} - \Delta_{\text{calc}})}{\sigma_{\Delta_i}^{\text{exp}}} \right\}^2 \right] \quad (6)$$

where Ψ_{exp} , Ψ_{calc} and Δ_{exp} , Δ_{calc} are the measured (experimental) and calculated ellipsometry functions, N is the number of measured Ψ , Δ pairs, M is the number of fitted parameters in the optical model and σ are standard deviations of the experimental data points [25,33].

In order to extract optimal data from SE experimental and simulated measurements, the construction of a multilayer optical model is essential. The model representation accounts for a number of distinct layers with individual optical dispersions and the interfaces between these layers are optical boundaries at which light is refracted and reflected according to the Fresnel relations. The dispersion relations of the optical constants of HfO_2 films are derived using a stack model composed of the Si substrate, interfacial SiO_2 layer, and HfO_2 film; the surface roughness was also considered to obtain precision during experimental fitting. Succeeding the construction of the optical layer model, the HfO_2 films were modeled with a conventional Cauchy dispersion model, because the films are transparent in the visible region the Cauchy model is optimal. The Cauchy equation can be expressed approximately as a refractive index n as a function of wavelength λ :

$$n(\lambda) = A + B/\lambda^2 + C/\lambda^4 \quad (7)$$

where A , B , and C are the Cauchy coefficients and specific to the material, A is the constant that dominates $n(\lambda)$ for long wavelengths, B controls the curvature of $n(\lambda)$ in the middle of the visible spectrum, and C influences $n(\lambda)$ to a greater extent in shorter wavelengths [31]. Note that this principle behind Cauchy's polynomial is also used for the dispersion function $k(\lambda)$:

$$k(\lambda) = d + e/\lambda^2 + f/\lambda^4 \quad (8)$$

where d , e , and f are constants specific to the material [26,37].

Microstructural information obtained from SE data for the HfO_2 films is film thickness, which is relative to the stack optical model. The variation of film thickness as a function of growth temperature for various crystalline HfO_2 films is shown in Fig. 11. It is evident that the film thickness is more or less constant with increasing growth temperature; this observation is consistent with XRR and SE for the crystalline samples. To validate the SE analysis and microstructure, the film thickness values obtained from SEM measurements are also plotted in Fig. 11. Distinct film properties are responsible for film thickness characterization, and ultimately it can be seen that the film thickness obtained from SE, XRR, and SEM are in reasonable agreement with respect to one another for

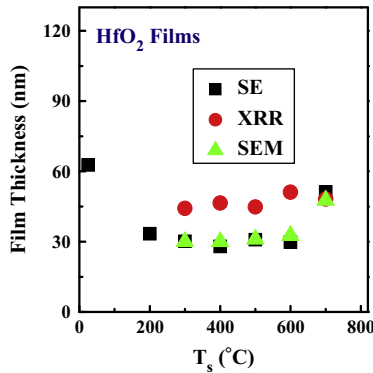


Fig. 11. Thickness measurements obtained through XRR, RBS, and SE modeling. The measurements commensurate with one another and deposition rate. Characterization techniques are then concluded to be highly satisfactory in obtaining other film properties, such as the optical constants, or chemical inertness in the films.

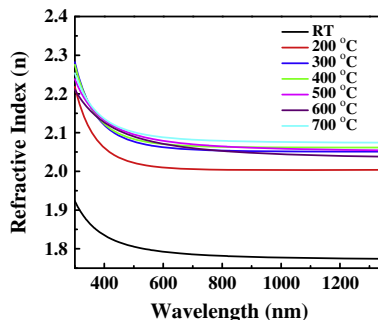


Fig. 12. The index of refraction profiles of HfO_2 films grown at various T_s . The effect of growth temperature is evident in the dispersion curves; 'n' values increase with T_s .

the monoclinic HfO_2 films. This observation indicates that the model(s) and SE analysis adopted can reasonably simulate the microstructure and, hence, optical properties of the sputter-deposited HfO_2 films.

The dispersion profiles of $n(\lambda)$ determined from SE data for the HfO_2 films are shown in Fig. 12. The $n(\lambda)$ dispersion curves indicate a sharp increase at shorter wavelengths corresponding to fundamental absorption of energy across the band gap. However, the effect of growth temperature is evident in the dispersion curves (Fig. 11), where there is an increase in 'n' with T_s . In order to further study the effect of growth temperature on the optical constants, the refractive index variation of the films at $\lambda = 550 \text{ nm}$ with growth temperature is shown in Fig. 13. At a $\lambda = 550 \text{ nm}$, the 'n' values increase from 1.79 to 2.09 with increasing growth temperature from 25 to 700 °C. The temperature dependence on structure is evident in the measurements where 'n' values increase drastically between the amorphous and monoclinic transformation of HfO_2 . Note that the 'n' value increases sharply with T_s initially and begins to depend less at higher T_s . However, the values obtained for the films are slightly less than the reported bulk value for HfO_2 [38] which can be attributed to the method of growth; the sputtered films are well known to have a higher defect density than bulk HfO_2 .

A simple model can be formulated to explain the effect of microstructure on the optical properties in HfO_2 films. Evident from the results and analysis, the optical quality of the HfO_2 films depends on the growth temperature and, hence, the film-microstructure. XRD measurements demonstrated that the HfO_2 films grown at $T_s = \text{RT}-700 \text{ °C}$ exhibit two sets of broad features from a structure point of view: amorphous and nanocrystalline. The

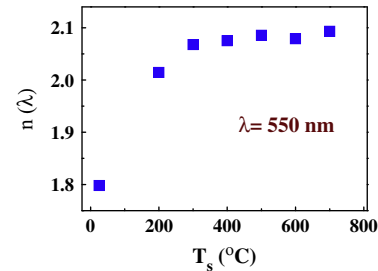


Fig. 13. Variation of 'n' ($\lambda = 550 \text{ nm}$) with T_s is shown in the insert. It is evident that the 'n' increases from 1.79 to 2.09 with increasing T_s from 25 to 700 °C.

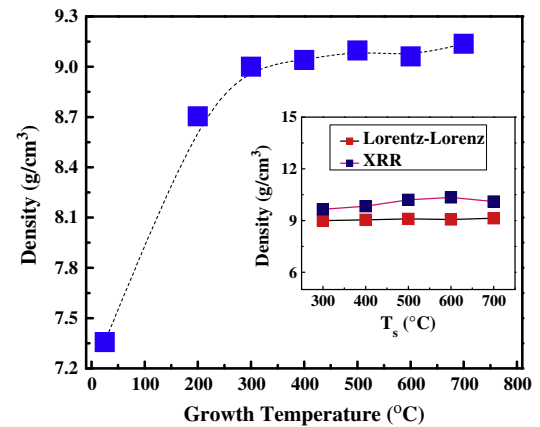


Fig. 14. Density measurements obtained from the Lorentz–Lorenz relation, as well as a correlation with XRR measurements.

nanocrystalline HfO_2 films crystallize in monoclinic structure. Furthermore, increasing T_s results in improved structural order and texturing of HfO_2 films along with an increase in the average crystallite size. The density of the film also increases, as evidenced by XRR analyses. It is well known that the refractive index is closely related to the physical properties and density of the films. Thus, the observed increase in 'n' values when HfO_2 films grown at higher T_s can be attributed to the improved packing density of the films coupled with improved structural order. Improved structural order results in the formation of a dense network of nanocrystals leading to an enhancement in the packing density. This characteristic change in structure results in the observed enhancement in 'n'. In order to further confirm the proposed physics and mechanism, the relative density of the film is also approximated using the Lorentz–Lorenz relation employing the measured 'n' values at 550 nm [39,40]. The functional dependence of the relative density of HfO_2 films on T_s is shown in Fig. 14. The density measured for amorphous HfO_2 films at $T_s = \text{RT}$ is only $7.4 \text{ g}/\text{cm}^3$. However, the density increases to $9.1 \text{ g}/\text{cm}^3$ for nanocrystalline HfO_2 films deposited at $T_s = 300\text{--}700 \text{ °C}$. XRR density measurements commensurate with the values derived from Lorentz–Lorenz relation as seen for the crystalline samples Fig. 14 (inset).

4. Conclusions

HfO_2 thin films were grown by sputter-deposition in a wide range of growth temperature, 25–700 °C. GIXRD studies revealed that the HfO_2 films deposited at $T_s < 200 \text{ °C}$ were amorphous while those grown at $T_s \geq 200 \text{ °C}$ were nanocrystalline and exhibit monoclinic structure. The detailed analyses based on XRD indicate that the average crystallite size of HfO_2 film increases from $\sim 10 \text{ nm}$

to ~20 nm with increasing T_s . The corresponding film roughness follows a decreasing trend with increasing T_s . The packing density and structural order of the HfO₂ films increases with increasing T_s . The band gap values of the HfO₂ films were found to be in the range of 5.78–6.17(±0.03) eV for T_s = 25–700 °C. The index of refraction and their dispersion profiles correlate with the microstructure.

Acknowledgements

The authors at the University of Texas at El Paso (UTEP) acknowledge with pleasure the support of the Air Force Research Laboratory (AFRL) (Contract Number: FA8650-05-D-1912) to perform this research work. M. Vargas also acknowledges the support from National Science Foundation (NSF); NSF-PREM Grant # DMR-1205302.

References

- [1] M.F. Al-Kuhaili, Opt. Mater. 27 (2004) 383–387.
- [2] N.C. Das, N.K. Sahoo, D. Bhattacharyya, S. Thakur, N.M. Kamble, D. Nanda, S. Hazra, J.K. Bal, J.F. Lee, Y.L. Tai, C.A. Hsieh, J. Appl. Phys. 108 (2010) 023515.
- [3] M. Liu, Q. Fang, G. He, L.Q. Zhu, L.D. Zhang, Appl. Surf. Sci. 252 (2006) 8673–8676.
- [4] J.M. Khoshman, M.E. Kordesch, Surf. Coat. Technol. 201 (2006) 3530–3535.
- [5] B. Aguirre, R.S. Vemuri, D. Zubia, M.H. Engelhard, V. Shuththanandan, K. Kamala Bharathi, C.V. Ramana, Appl. Surf. Sci. 257 (2011) 2197–2202.
- [6] M.F. Al-Kuhaili, S.M.A. Durrani, I.A. Bakhtiari, M.A. Dastageer, M.B. Mekki, Mater. Chem. Phys. 126 (2011) 515–523.
- [7] X. Luo, W. Zhou, S.V. Ushakov, A. Navrotsky, A.A. Demkov, Phys. Rev. B 80 (2009) 134119.
- [8] E.-C Kang, K.J. Lee, Phys. Rev. B 68 (2003) 054106.
- [9] T.J. Bright, J.I. Watjen, Z.M. Zhang, C. Muratore, A.A. Voevodin, Thin Solid Films 520 (2012) 6793–6802.
- [10] A. Ortega, E.J. Rubio, K. Abhilash, C.V. Ramana, Opt. Mater. 35 (2013) 1728–1734.
- [11] P. Torchio, A. Gatto, M. Alvisi, G. Albrand, N. Kaiser, C. Amra, Appl. Opt. 41 (2002) 3256–3261.
- [12] E. Filatova, A. Sokolov, J.-M. Andre, F. Schaefers, W. Braun, Appl. Opt. 49 (2010) 2539–2546.
- [13] M. Vargas, N.R. Murphy, C.V. Ramana, Appl. Phys. Lett. 104 (2014) 101907.
- [14] L. Gallais, J. Capoulade, J.Y. Natoli, M. Commandre, M. Cathelinaud, C. Koc, M. Lequime, Appl. Opt. 47 (2008) C107–C113.
- [15] S.M.A. Durrani, Sens. Actuators, B 120 (2007) 700–705.
- [16] B.D. Cullity, S.R. Stock, Elements of X-Ray Diffraction, third ed., Prentice-Hall Inc., 2001.
- [17] D.-M. Smligies, Appl. Cryst. 42 (2009) 1030–1034.
- [18] Bruker Application Note #133: Introduction to Bruker's ScanAsyst and PeakForce Tapping AFM Technology (<http://www.bruker.com/products/surface-analysis/atomic-force-microscopy/modes/modes-techniques/primary-modes/scanasyst.html?gclid=CP7Ew9GU1r0CFQUjvAodfhkAbQ>).
- [19] M.-Y. Ho, H. Gong, G.D. Wilk, B.W. Busch, M.L. Green, P.M. Voyles, D.A. Muller, M. Bude, W.H. Lin, A. See, M.E. Loomans, S.K. Lahiri, P.I. Raisanen, J. Appl. Phys. 93 (2003) 1477–1481.
- [20] C.V. Ramana, K.K. Bharathi, A. Garcia, A.L. Campbell, J. Phys. Chem. C 116 (2012) 9955–9960.
- [21] A.B. Mukhopadhyay, J.F. Sanz, C.B. Musgrave, Phys. Rev. B. 73 (2006) 115330.
- [22] S.M. Haque, P.R. Sagdeo, S. Balaji, K. Sridhar, S. Kumar, D. Bhattacharyya, D. Bhattacharyya, N.K. Sahoo, J. Vac. Sci. Technol., B 32 (2014) 03D104.
- [23] A. Callegari, E. Cartier, M. Gribelyuk, H.F. Okorn-Schmidt, T. Zabel, J. Appl. Phys. 90 (2001) 6466.
- [24] L. Pereira, P. Barquinha, E. Fortunato, R. Martins, Mater. Sci. Eng., B 118 (2001) 210–213.
- [25] C.V. Ramana, G. Baghmar, E.J. Rubio, M.J. Hernandez, ACS Appl. Mater. Interf. 5 (2013) 4659–4666.
- [26] V.H. Mudavakkat, V.V. Atuchin, V.N. Kruchinin, A. Kayani, C.V. Ramana, Opt. Mater. 34 (2012) 893–900.
- [27] M.C. Cisneros-Morales, C.R. Aita, Appl. Phys. Lett. 96 (2010) 191904.
- [28] J.-W. Park, D.-K. Lee, D. Lim, H. Lee, S.-H. Choi, Appl. Phys. Lett. 104 (2008) 033521.
- [29] J. Aarik, H. Mandar, M. Kirm, L. Pung, Thin Solid Films 466 (2004) 41–47.
- [30] F.L. Martinez, M. Toledoano-Luque, J.J. Gandia, J. Carabe, W. Bohne, J. Rohrich, E. Strub, I. Martil, J. Phys. D Appl. Phys. 40 (2007) 5256–5265.
- [31] I. Kosacki, V. Petrovsky, H.U. Anderson, Appl. Phys. Lett. 74 (1999) 341–343.
- [32] J. Kang, E.-C. Lee, K.J. Chang, Phys. Rev. B. 68 (2003) 054106.
- [33] G.E. Jellison Jr., Thin Solid Films 290–291 (1996) 40–45.
- [34] H. Fujiwara, Spectroscopic Ellipsometry: Principles and Applications, John Wiley & Sons Inc., 2007.
- [35] O. Auciello, A.R. Krauss, In-Situ Real Time Characterization of Thin Films, John Wiley & Sons Incorporated, New York, 2001.
- [36] J.A. Woollam Co., Incorporated, Guide to Using WVASE32 Spectroscopic Ellipsometry Data Acquisition and Analysis Software, Copyright 1994–2008.
- [37] T. Tan, Z. Liu, H. Lu, W. Liu, H. Tian, Opt. Mater. 32 (2010) 432–435.
- [38] H. Hu, C. Zhu, Y.F. Lu, Y.H. Wu, T. Liew, M.F. Li, B.J. Cho, W.K. Choi, N. Yakovlev, J. Appl. Phys. 94 (2003) 551–557.
- [39] M.F. Al-Kuhaili, M. Saleem, S.M.A. Durrani, J. Alloys Compd. 521 (2012) 178–182.
- [40] O. Stenzel, The Physics of Thin Film Optical Spectra: An Introduction, Springer-Verlag, Berlin Heidelberg, Germany, 2005.